

## Dimensional control of defect dynamics in perovskite oxide superlattices

Isaac Bredeson,<sup>1</sup> Lipeng Zhang,<sup>1</sup> P. R. C. Kent,<sup>2,3</sup> Valentino R. Cooper,<sup>4</sup> and Haixuan Xu (徐海韻)<sup>1,5,\*</sup>

<sup>1</sup>*Department of Materials Science and Engineering, The University of Tennessee, Knoxville, Tennessee 37996, USA*

<sup>2</sup>*Center for Nanophase Materials Science, Oak Ridge National Laboratory, Oak Ridge, Tennessee 37831, USA*

<sup>3</sup>*Computational Science and Engineering Division, Oak Ridge National Laboratory, Oak Ridge, Tennessee 37831, USA*

<sup>4</sup>*Materials Science and Technology Division, Oak Ridge National Laboratory, Oak Ridge, Tennessee 37831, USA*

<sup>5</sup>*Joint Institute for Advanced Materials, The University of Tennessee, Knoxville, Tennessee 37996, USA  
and Oak Ridge National Laboratory, Oak Ridge, Tennessee 37831, USA*



(Received 2 December 2017; published 8 March 2018)

Point defects play a critical role in the structural, physical, and interfacial properties of perovskite oxide superlattices. However, understanding of the fundamental properties of point defects in superlattices, especially their transport properties, is rather limited. Here, we report predictions of the stability and dynamics of oxygen vacancies in SrTiO<sub>3</sub>/PbTiO<sub>3</sub> oxide superlattices using first-principles calculations in combination with the kinetic Monte Carlo method. By varying the stacking period, i.e., changing of  $n$  in  $n$ STO/ $n$ PbTO, we discover a crossover from three-dimensional diffusion to primarily two-dimensional planar diffusion. Such planar diffusion may lead to novel designs of ionic conductors. We show that the dominant vacancy position may vary in the superlattices, depending on the superlattice structure and stacking period, contradicting the common assumption that point defects reside at interfaces. Moreover, we predict a significant increase in room-temperature ionic conductivity for 3STO/3PbTO relative to the bulk phases. Considering the variety of cations that can be accommodated in perovskite superlattices and the potential mismatch of spin, charge, and orbitals at the interfaces, this paper identifies a pathway to control defect dynamics for technological applications.

DOI: [10.1103/PhysRevMaterials.2.035401](https://doi.org/10.1103/PhysRevMaterials.2.035401)

### I. INTRODUCTION

Oxide superlattices exhibit some novel properties and phenomena that their bulk counterparts do not, primarily due to the delicate electronic and magnetic interactions as well as lowered symmetry in the interfacial region [1–8]. For instance, a high-mobility, two-dimensional electron gas was achieved between two insulators (SrTiO<sub>3</sub> and LaAlO<sub>3</sub>) [9] and polar vortices have been observed in SrTiO<sub>3</sub>/PbTiO<sub>3</sub> (STO/PbTO) [10]. In addition, oxide superlattices have shown other unprecedented physical properties for technologically important applications, e.g., colossal electrical conductivity in superlattices consisting of SrTiO<sub>3</sub> and yttrium stabilized zirconia [11], and strong polarization enhancement in SrTiO<sub>3</sub>/BaTiO<sub>3</sub>/CaTiO<sub>3</sub> [12]. The interfaces created in these superlattices play a critical role in influencing physical properties.

While many studies have focused on the interface [13], e.g., symmetry lowering and the unavoidable influence from point defects [14], an understanding of defect properties, especially defect transport properties, and how to control them in oxide superlattices is limited. One challenge is the difficulty of dynamically tracking the trajectories of these point defects due to the time scales involved as they are too fast for experimental techniques and too slow for direct atomistic molecular dynamics simulations. In addition, these systems are complicated by the correlations between octahedral rotations, polarization, and electronic and magnetic structure [15,16], which require investigation of a large phase space of materials

parameters. Nevertheless, point defects are key to physical and interfacial properties of oxide superlattices [17,18]. The ability to manipulate oxygen vacancies is essential for practical applications, such as ferroelectric memory [12], field-effect devices [19], solid oxide fuel cells [20], and pseudocapacitors [21].

Here, the formation energies and transport behavior of charged oxygen vacancies (+2) are examined in the paraelectric and ferroelectric phases of  $n$ SrTiO<sub>3</sub>/ $n$ PbTiO<sub>3</sub> ( $n$ STO/ $n$ PbTO,  $n = 1, 2, 3, 4$ ) superlattices, a prototypical perovskite ferroelectric superlattice. We use density functional theory in combination with kinetic Monte Carlo (KMC) simulations to compute the stability and dynamics of oxygen vacancies. The statistically time-averaged defect positions along the stacking direction of the superlattices are determined. The site preferences are compared among superlattices ( $n$ STO/ $n$ PbTO), which allows for an examination of trends in properties for superlattices of varying stacking orders. The oxygen vacancy diffusivities at various temperatures and the effective migration energy barriers (MEBs) are calculated based on the oxygen vacancy trajectories.

### II. METHODOLOGY AND COMPUTATIONAL DETAILS

The Vienna *ab initio* simulation package (VASP) [22] was employed to determine the defect properties. The exchange-correlation functional of the calculation was the revised version Perdew-Burke-Ernzerhof for solids (PBEsol) [23] with the generalized gradient approximation. The valence electrons of the atoms were set as Sr 4s4p5s, Pb 5d6s6p, Ti 3p3d4s, and O 2s2p orbital electrons. The cutoff energy was set to 550 eV based on convergence tests. A 2×2×2 Monkhorst-Pack

\*xhx@utk.edu

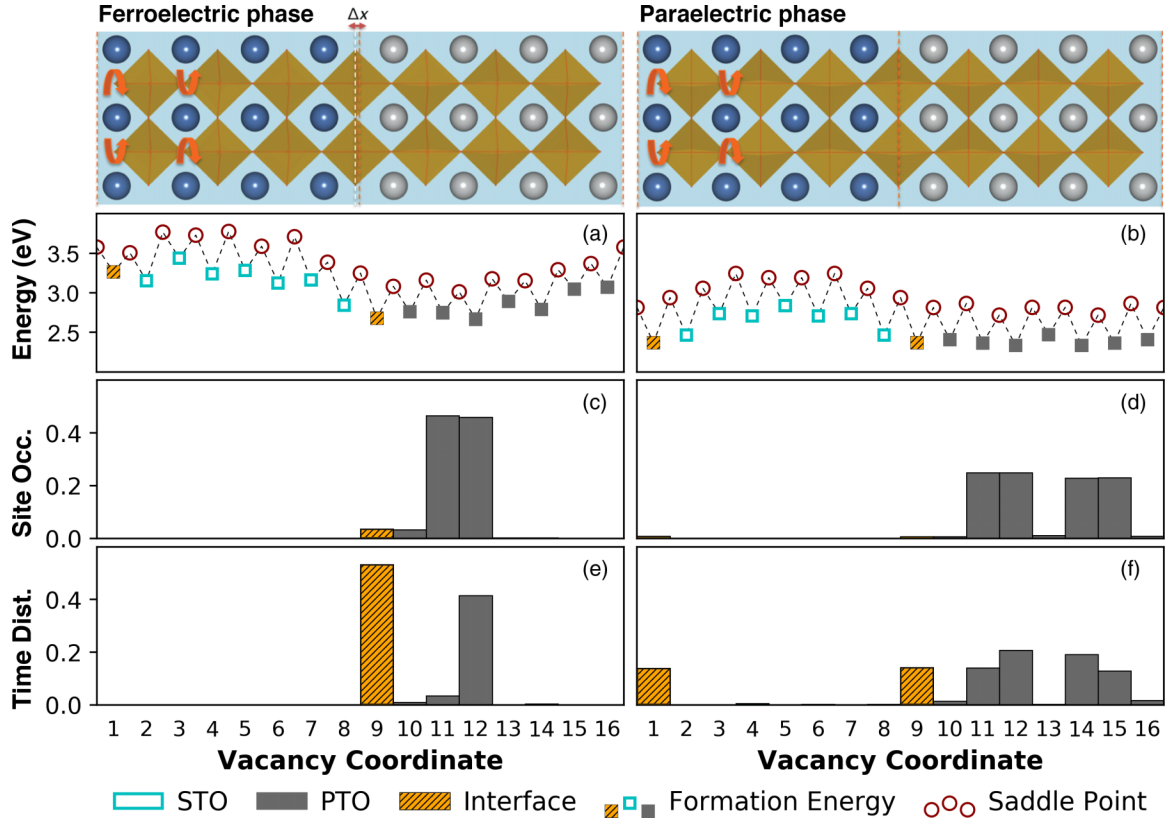


FIG. 1. Top: Crystal structure of ferroelectric and paraelectric 4STO/4PTO oxide superlattices. (a, b) The defect formation energies and migration energy barriers of each phase, respectively. (c, d) Site occupancy of an oxygen vacancy in ferroelectric and paraelectric 4STO/4PTO. (e, f) Time distribution representing in which layer the defect spends most of its time. The interfacial  $\text{TiO}_2$  layers are highlighted in orange color.

$k$ -point scheme was used, which yielded numerical accuracy within 1 meV of the total-energy differences compared to denser  $k$ -point grids. Full relaxations of the superlattices were performed until all the Hellmann-Feynman forces were smaller than 0.01 eV/Å.

The STO/PTO superlattices were built by stacking equally thick layers of  $\text{SrTiO}_3$  and  $\text{PbTiO}_3$  on one another with varying thicknesses from  $n = 1$  to 4 to form  $n\text{STO}/n\text{PTO}$  structures. A side view of the 4STO/4PTO structure is shown in Fig. 1 (top). The total thickness of the  $n = 1, 2$ , and 4 structures was eight unit cells, with six unit cells for the 3STO/3PTO structure. For  $n = 1, 2, 4$  there are 16 total layers of oxygen sites and 12 total layers for  $n = 3$ . In addition, two tetragonal reference structures were built of bulk STO and bulk PTO. For all structures, the  $x, y$  size was set to  $2\sqrt{2} \times 2\sqrt{2}$  and the in-plane lattice constant was set to be 3.898 Å, the same as bulk  $\text{SrTiO}_3$ , to mimic the effects of superlattices on a STO substrate. The  $c/a$  ratio was systematically relaxed for each of the superlattices and reference structures.

The single oxygen vacancy formation energy was calculated via

$$E_f(V_O^q) = E_{\text{tot}}(V_O^q) - E_{\text{tot}}(\text{perfect}) + \mu + q(E_f + E_v + \Delta V)$$

where  $E_{\text{tot}}(V_O^q)$  is the total energy of the defective superlattice with one oxygen vacancy in charge state  $q$ , in this paper  $q = +2$ .  $E_{\text{tot}}(\text{perfect})$  is the total energy of the perfect

superlattice, and  $\mu$  is the chemical potential of oxygen as calculated by VASP, set to half of the equilibrium gas state,  $1/2 E(\text{O}_2)$ ,  $-4.388$  eV in this case.  $E_F$  is the Fermi level with respect to the valence-band maximum, which is set as the middle value between the valence-band maximum and conduction-band minimum of the perfect superlattice.  $\Delta V$  is the correction term used to align the reference potential in the defective and perfect superlattices. The climbing nudged elastic band [24] method was used to obtain the MEBs.

An atomistic kinetic Monte Carlo model [25–28] was built based on the lattices of the oxide superlattices with periodic boundary conditions (PBCs). During the simulation, a vacancy is moved to an available neighboring vacancy site each iteration according to probabilities calculated from MEBs. There are two kinds of layers that alternate:  $\text{TiO}_2$ , and AO ( $A = \text{Sr}$  or  $\text{Pb}$ ) layers having either Sr or Pb. Each oxygen vacancy site has eight possible diffusion paths. Sites on  $\text{TiO}_2$  layers have two paths up, two down, and four lateral paths. Sites on AO layers have four paths up and four paths down. Each of these path directions have a diffusion energy barrier value, but the barrier is equal among the individual paths of the same direction due to symmetry. Diffusion constants are related to MEB based on the Arrhenius equation:

$$D = D_0 e^{-\frac{E_m}{k_b T}}$$

where  $D$  is the diffusion coefficient,  $D_0$  is the prefactor,  $E_m$  is the MEB,  $k_b$  is Boltzmann's constant, and  $T$  is the temperature.

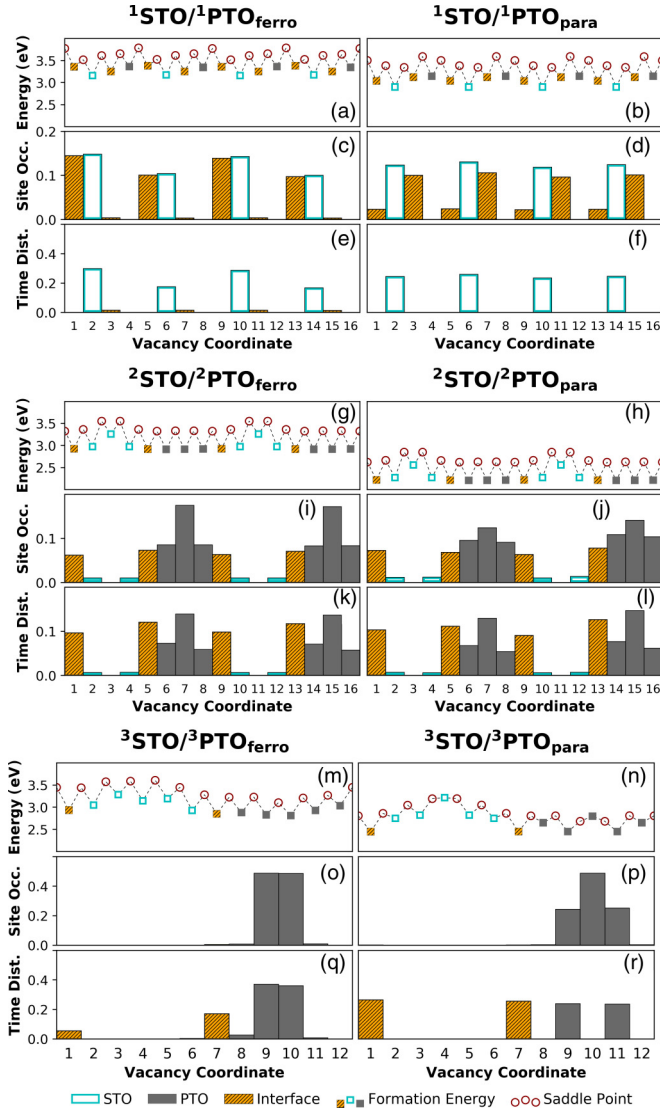


FIG. 2. The formation energies and energy barriers (a, b, g, h, m, n) were used in the KMC simulation. The normalized histogram of the total number of iterations the defect spent at each layer is shown in panels (c, d, i, j, o, p), and the total time at each layer is shown in panels (e, f, k, l, q, r). The defect layer is denoted here as the vacancy coordinate.

The probability of an oxygen defect is calculated using jump frequency for one specific path divided by the total jump frequency for all possible paths:

$$P_i = \frac{f_i}{\sum_{i=1,2,\dots,8} f_{\text{Total}}}$$

where  $P_i$  is the probability of a defect moving along a specific path,  $f_i$  is the jump frequency for that path, and the sum of  $f_{\text{Total}}$  is the sum of the jump frequency for all available paths. The defect is moved every iteration according to those probabilities. The defect position is recorded each iteration, the totals for which are normalized to get the site occupancy as in panels (c) and (d) in Figs. 1 and 2.

The time that a defect occupies a certain position is based on the residence time algorithm and the attempt frequency

is assumed to be  $10^{12}\text{s}^{-1}$  in this paper. The time spent at a particular defect layer is tallied then normalized to get the time distribution as in panels (e) and (f) in Figs. 1 and 2. The site occupancy and time distribution were calculated for each structure by initializing a single defect for  $10^6$  iterations. This process was done once for each defect layer each time initializing the defect on a different layer so that every layer had a run with the defect starting on it for a total of  $16 \times 10^6$  iterations for  $n = 1, 2, 4$ , and  $12 \times 10^6$  iterations for  $n = 3$ . This allowed for statistical convergence on all structures except for the 1STO/1PTO ferroelectric structure, which required  $16 \times 10^7$  iterations to converge.

Diffusivity was calculated from MSD via

$$D = \frac{\text{MSD}}{6 \cdot \Delta t}$$

where  $\Delta t$  is the total time for the 50-step interval over which the MSD was calculated. The average and standard error were calculated for each set of diffusivity calculations. This calculation was performed on data simulated between 300 and 700 K at 20-deg intervals, then plotted in an Arrhenius plot.

### III. RESULTS AND DISCUSSION

We begin by discussing the defect formation energies ( $\Delta E_f$ ) and MEBs of an oxygen vacancy in paraelectric and ferroelectric 4STO/4PTO superlattices (Fig. 1), along with their crystal structures, normalized time distribution at each site, and the frequency of each site being visited. In this system, the interface layer is defined as the  $\text{TiO}_2$  layer lying between two AO layers with different types of metal ions (Sr versus Pb). For the centrosymmetric paraelectric phase, the formation energies are symmetric with respect to their structurally equivalent positions. As a result, both interfaces [layer 1 and 9 in Fig. 1(b)] possess the same formation energies. In comparison, the ferroelectric phase exhibits an asymmetric formation energy curve, due to the breaking of centrosymmetry. The ferroelectric system is essentially composed of two different interfaces which exhibit substantially different oxygen vacancy formation energies [Fig. 1(a)];  $\Delta E_f$  of interface layer 1 exhibits a much higher value than the  $\Delta E_f$  at layer 9. This difference depends on the direction of the polarization [from left to right pointing towards layer 9 in Fig. 1(a)] in the system. Reversing the polarization direction will result in swapping of  $\Delta E_f$  at these two interfaces (layer  $9 > \text{layer } 1$ ). Compared with the reference constituent oxides in tetragonal structures, the formation energies in ferroelectric and paraelectric 4STO/4PTO are lower. Here, octahedral rotations play a critical role for this change in the PTO region of the superlattice, decreasing the formation energy by as much as  $\sim 0.4$  eV.

The saddle points at symmetrically equivalent positions in the paraelectric 4STO/4PTO are comparable to each other, with essentially the same MEBs. The oxygen vacancy time-averaged position is found to be within PTO layers based on the site and time distribution, rather than in the speculated interfacial layer. For ferroelectric 4STO/4PTO, the saddle points are distinctively different from that in the paraelectric phase and the vacancy is favorable near the interface (layer 9), primarily between layers 9 and layer 12 (in the PTO component). This indicates an accumulation of oxygen vacancies near one of



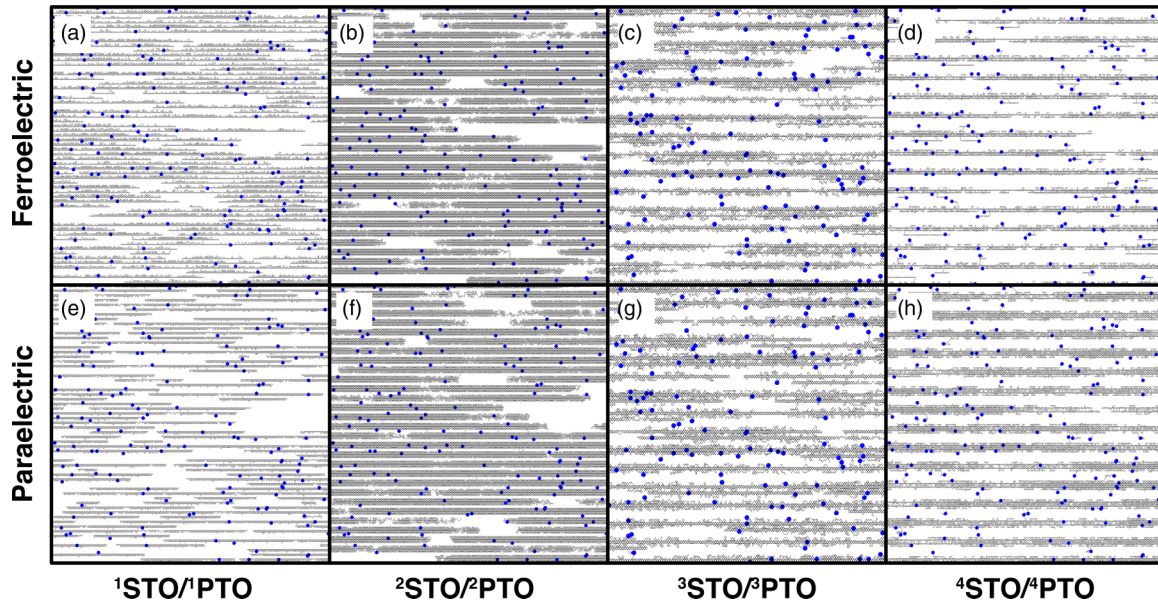


FIG. 3. Trajectories of 300 oxygen vacancies in  $60\sqrt{2} \times 60\sqrt{2} \times 80$  superlattices at 300 K with different stacking period as seen from the side, assuming no defect-defect interaction. Initial defect locations are shown as blue dots, with black lines showing the motion of each defect over the 10000 iteration simulation.

the interfaces and a depletion at the other in the ferroelectric systems. A consequence is that changes in the direction of the polarization can have significant effects on the materials' defect distributions.

To reveal the statistically time-averaged position of an oxygen vacancy at finite temperatures in other superlattices, the site occupancies and time distribution of an oxygen vacancy in  $n$ STO/ $n$ PTO ( $n = 1, 2, 3$ ) from the KMC simulations are shown in Fig. 2. In comparing the KMC results across all stacking periods, we see almost all systems exhibit some preference for STO layers or PTO layers, with PTO strongly preferred for  $n = 2, 3, 4$ , and a transition to a strong preference for the STO layer when  $n = 1$ , indicating the 1STO/1PTO system may be different from the rest of the superlattices [1]. This material preference leads to some degree of confinement for all systems.

The polarization effects (ferroelectric versus paraelectric) on defect properties are also evaluated. For 1STO/1PTO, the ferroelectric phase and paraelectric phase have different preferred interfaces as seen in the site distribution (Fig. 2), but in both instances the defect spends a negligible amount of time on the PbO layers. Interestingly, the ferroelectric and paraelectric 2STO/2PTO systems are similar to one another, with the only significant difference being in the center PTO layer 7 (and 15 due to PBC), with the defect spending more iterations on these layers in the ferroelectric system versus the paraelectric system. In 3STO/3PTO the ferroelectric system differs from the paraelectric in interface preference, similar to the 4STO/4PTO systems. The defects in the ferroelectric system strongly prefer the layer 7 interface versus the layer 1 interface, whereas both interface layers 1 and 7 in the paraelectric system are equally preferred. There is also a significant difference in defect confinement in the ferroelectric versus paraelectric systems in 3STO/3PTO, with the ferroelectric system showing strong confinement to only layers 9 and 10,

whereas the defect in the paraelectric system moves relatively freely along the entire PTO layer including each interface. A qualitative illustration of these effects is shown in Fig. 3. Together with the site occupancy and time distribution, our results demonstrate that the dominant sites are governed by the stacking period and superlattice phase (i.e., ferroelectric or paraelectric).

For defect transport properties, we find that the oxygen vacancy diffusion is mainly two-dimensional in some of the superlattices, such as ferroelectric 4STO/4PTO and ferroelectric 1STO/1PTO, as shown in Fig. 3. By combining both the defect site occupancy and transport properties, we find that the two-dimensional diffusion is caused by the high anisotropy of MEBs and geometrical constraints in the superlattice, as shown in Fig. 4. For instance, the MEBs along different paths from the same initial position, e.g., layer 7 in Fig. 4(a), vary as much as  $\sim 0.3$  eV in the ferroelectric 4STO/4PTO. The diffusion anisotropy in the PTO component of superlattices is much higher than the chosen reference PTO systems and cannot be simply explained by the  $c/a$  ratio of the tetragonal supercell. In addition, oxygen vacancy diffusion is geometrically constrained in these superlattices. For instance, an oxygen vacancy can only move out-of-plane in an AO layer. In contrast, an oxygen vacancy can diffuse in-plane or out-of-plane in the  $\text{TiO}_2$  layers. This leads to competition between different diffusion paths, e.g., in-plane versus out-of-plane. Taking a vacancy in the odd-numbered  $\text{TiO}_2$  layers of 1STO/1PTO as an example, the diffusion path away from this layer (along the  $z$  direction) has a lower MEB than the paths associated with the in-plane diffusion; however, the subsequent diffusion predominantly leads to a backwards jump to the  $\text{TiO}_2$  layer. Therefore, the vacancy is trapped in these layers at room temperatures. In this case, the KMC model reveals that the effective barrier is determined by both the in-plane and out-of-plane diffusion.

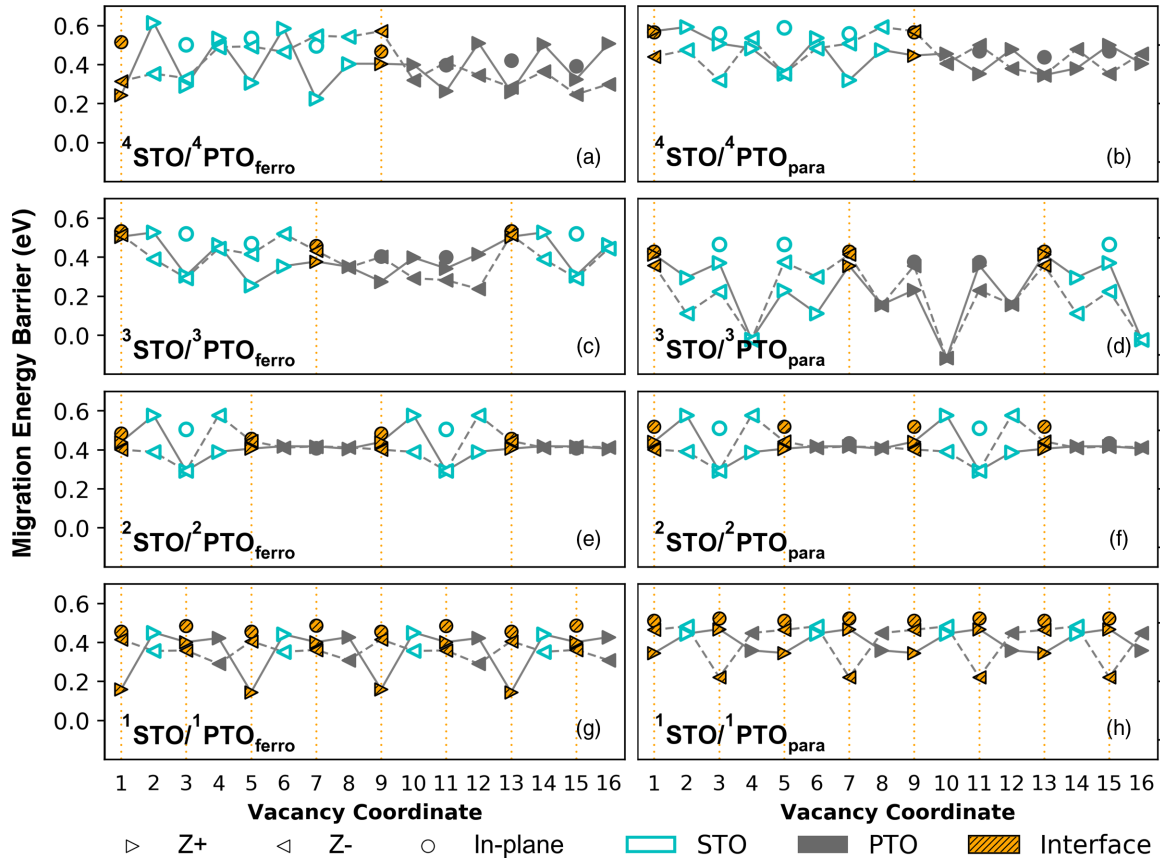


FIG. 4. Migration energy barriers along different directions in STO/PTO superlattices.  $Z + / Z -$  is the energy barrier for a defect to move to a higher/lower defect layer, respectively. The defect layer is denoted here as the vacancy coordinate.

By comparing different superlattices, we notice significant variance in the MEB profile as the stacking period of superlattices changes. For instance, for **2STO/2PTO**, the diffusion anisotropy is almost completely suppressed in the PTO layers (Fig. 4); all corresponding diffusion paths have indistinguishable MEBs. In contrast to all other investigated systems, the defect transport properties in ferroelectric and paraelectric **2STO/2PTO** are similar to each other [Fig. 4(e) versus Fig. 4(f)], indicating little coupling to the polarization. For both ferroelectric and paraelectric **1STO/1PTO**, the anisotropic diffusion in one of the interfaces is significantly larger than the other. It should be noted that the interfacial effects may strongly overlap in the **1STO/1PTO** system, in which the interfaces are in close proximity to each other.

The diffusivities calculated based on the mean square displacements of various oxide superlattices are shown in Fig. 5 as a function of temperature. At 300 K, the variation in diffusivity among different superlattices covers multiple orders of magnitude. We observe that paraelectric **3STO/3PTO** shows the highest diffusivity in comparison with bulk systems and other superlattices. While the diffusivity is found to be rather sensitive to the structure itself, no systematic trend is observed as the number of layers in the superlattices increases. The diffusivity in the ferroelectric **1STO/1PTO** system is approximately one order of magnitude higher at 300 K than that of **2STO/2PTO**, but has a similar diffusivity as ferroelectric **4STO/4PTO**.

The diffusivities can be directly linked to differences in the effective migration barriers of different superlattices. As can be determined from the extrapolated Arrhenius relationship, these vary significantly; approximately 0.2 eV difference was found among these systems. Paraelectric **3STO/3PTO** shows the smallest effective MEB, which is also smaller than that of the reference bulk STO and PTO. The ferroelectric **1STO/1PTO**

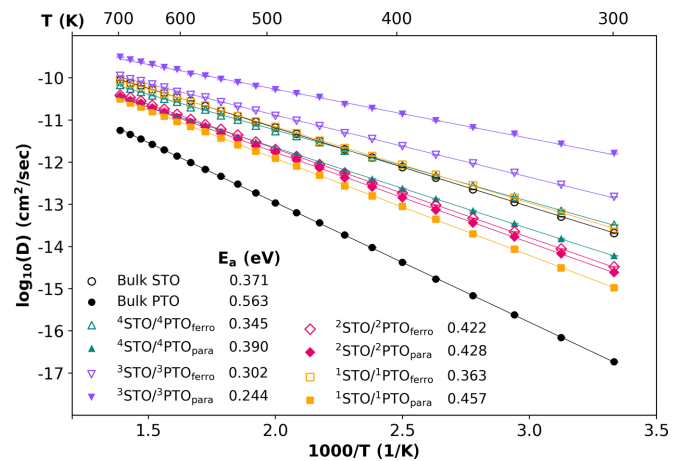


FIG. 5. Arrhenius plot of various STO/PTO superlattices with effective activation energies, in comparison with bulk reference data. Depending on the superlattice geometry and phase, diffusivity may be strongly enhanced or suppressed.

and 4STO/4PTO have similar MEBs, which are 0.345 and 0.363 eV, respectively. Despite the similar effective MEBs, the details of defect transport are fundamentally different and this demonstrates the importance of stacking order, as discussed previously. For instance, the effective MEB in the ferroelectric 4STO/4PTO is a statistically averaged result of multiple diffusion paths in several atomic layers of the PTO region; in comparison, the effective MEB in ferroelectric 1STO/1PTO is mostly determined by the diffusion barriers around the TiO<sub>2</sub> layer in the STO region.

#### IV. SUMMARY

The stability and dynamics of oxygen vacancies in SrTiO<sub>3</sub>/PbTiO<sub>3</sub> oxide superlattices are examined using density functional theory calculations combined with kinetic Monte Carlo simulations. We find that oxygen vacancy can be confined to a few atomic planes in some of these oxide superlattices, exhibiting essentially two-dimensional diffusion. The dominant defect position could reside in the bulk-like region as well as at the interfaces, depending on the stacking period and superlattice structure (ferroelectric versus paraelectric). Varying the stacking period also changed the preferred region of the material for the defect; the PTO region was preferred for stacking periods of  $n = 2, 3, 4$ , whereas the STO layers were preferred for the  $n = 1$  superlattice. Orders-of-magnitude increase in ionic conductivity from room temperature is also predicted in the 3STO/3PTO system relative to the bulk phases.

Considering the variety of cations that can be accommodated in perovskite superlattices and the potential mismatch of spin, charge, and orbitals at the interfaces, this paper identifies a

pathway for controlling defect dynamics in oxide superlattices. We expect that changing the  $B$ -site element (in  $ABO_3$ ) or  $A$  and  $B$  site simultaneously of superlattices may lead to enhanced ionic conduction and alternating stacking period with uneven number of layers of the constituent oxides ( $n$ STO/ $m$ PTO,  $n \neq m$ ) will provide further control of conduction. Given the high-quality oxide superlattices and epitaxial heterostructures that can be synthesized using current state-of-art fabrication techniques, we hope our predictions motivate experimental confirmation and further examination of defect transport properties using advanced characterization methods, e.g., *in situ* transmission electron microscopy [20].

#### ACKNOWLEDGMENTS

This research is sponsored by The University of Tennessee (UT) Science Alliance Joint Directed Research and Development Program (L.Z., I.B., and H.X.) and the Laboratory Directed Research and Development Program of Oak Ridge National Laboratory (V.R.C. and P.R.C.K.), managed by UT-Battelle, LLC, for the U.S. Department of Energy (DOE). This paper has been authored by UT-Battelle, LLC, under Contract No. DE-AC05-00OR22725 with the DOE. The U.S. Government is authorized to reproduce and distribute reprints for Governmental purposes. This research used resources of the National Energy Research Scientific Computing Center, a DOE Office of Science User Facility supported by the Office of Science of the DOE under Contract No. DE-AC02-05CH11231 and the National Institute for Computational Sciences at UT under Contract No. UT-TENN0112.

*Attributions.* I.B. and L.Z. contributed equally to this paper.

- 
- [1] E. Bousquet, M. Dawber, N. Stucki, C. Lichtensteiger, P. Hermet, S. Gariglio, J. M. Triscone, and P. Ghosez, *Nature (London)* **452**, 732 (2008).
  - [2] C. H. Ahn, K. M. Rabe, and J. M. Triscone, *Science* **303**, 488 (2004).
  - [3] J. Ravichandran, A. K. Yadav, R. Cheaito, P. B. Rossen, A. Soukiasian, S. J. Suresha, J. C. Duda, B. M. Foley, C. H. Lee, Y. Zhu, A. W. Lichtenberger, J. E. Moore, D. A. Muller, D. G. Schlom, P. E. Hopkins, A. Majumdar, R. Ramesh, and M. A. Zurbuchen, *Nat. Mater.* **13**, 168 (2014).
  - [4] P. Zubko, S. Gariglio, M. Gabay, P. Ghosez, and J. M. Triscone, *Annu. Rev. Condens. Matter Phys.* **2**, 141 (2011).
  - [5] P. Zubko, J. C. Wojdel, M. Hadjimichael, S. Fernandez-Pena, A. Sene, I. Luk'yanchuk, J. M. Triscone, and J. Iniguez, *Nature (London)* **534**, 524 (2016).
  - [6] N. Nakagawa, H. Y. Hwang, and D. A. Muller, *Nat. Mater.* **5**, 204 (2006).
  - [7] H. W. Jang, D. A. Felker, C. W. Bark, Y. Wang, M. K. Niranjan, C. T. Nelson, Y. Zhang, D. Su, C. M. Folkman, S. H. Baek, S. Lee, K. Janicka, Y. Zhu, X. Q. Pan, D. D. Fong, E. Y. Tsybal, M. S. Rzchowski, and C. B. Eom, *Science* **331**, 886 (2011).
  - [8] A. Brinkman, M. Huijben, M. Van Zalk, J. Huijben, U. Zeitler, J. C. Maan, W. G. Van der Wiel, G. Rijnders, D. H. A. Blank, and H. Hilgenkamp, *Nat. Mater.* **6**, 493 (2007).
  - [9] A. Ohtomo and H. Y. Hwang, *Nature (London)* **427**, 423 (2004).
  - [10] A. K. Yadav, C. T. Nelson, S. L. Hsu, Z. Hong, J. D. Clarkson, C. M. Schlepütz, A. R. Damodaran, P. Shafer, E. Arenholz, L. R. Dedon, D. Chen, A. Vishwanath, A. M. Minor, L. Q. Chen, J. F. Scott, L. W. Martin, and R. Ramesh, *Nature (London)* **534**, 138 (2016).
  - [11] J. Garcia-Barriocanal, A. Rivera-Calzada, M. Varela, Z. Sefrioui, E. Iborra, C. Leon, S. J. Pennycook, and J. Santamaria, *Science* **321**, 676 (2008).
  - [12] H. N. Lee, H. M. Christen, M. F. Chisholm, C. M. Rouleau, and D. H. Lowndes, *Nature (London)* **433**, 395 (2005).
  - [13] E. Fabbri, D. Pergolesi, and E. Traversa, *Sci. Technol. Adv. Mater.* **11**, 044301 (2010).
  - [14] D. A. Muller, N. Nakagawa, A. Ohtomo, J. L. Grazul, and H. Y. Hwang, *Nature (London)* **430**, 657 (2004).
  - [15] Y. J. Zhou and K. M. Rabe, *Phys. Rev. Lett.* **115**, 106401 (2015).
  - [16] A. Thess, *Phys. Rev. Lett.* **111**, 110602 (2013).
  - [17] F. Gunkel, C. Bell, H. Inoue, B. Kim, A. G. Swartz, T. A. Merz, Y. Hikita, S. Harashima, H. K. Sato, M. Minohara, S. Hoffmann-Eifert, R. Dittmann, and H. Y. Hwang, *Phys. Rev. X* **6**, 031035 (2016).
  - [18] B. W. Veal, S. K. Kim, P. Zapol, H. Iddir, P. M. Baldo, and J. A. Eastman, *Nat. Commun.* **7**, 11892 (2016).
  - [19] J. Mannhart and D. G. Schlom, *Science* **327**, 1607 (2010).

- [20] Y. M. Kim, J. He, M. D. Biegalski, H. Ambaye, V. Lauter, H. M. Christen, S. T. Pantelides, S. J. Pennycook, S. V. Kalinin, and A. Y. Borisevich, *Nat. Mater.* **11**, 888 (2012).
- [21] J. T. Mefford, W. G. Hardin, S. Dai, K. P. Johnston, and K. J. Stevenson, *Nat. Mater.* **13**, 726 (2014).
- [22] G. Kresse and J. Furthmuller, *Comp. Mater. Sci.* **6**, 15 (1996).
- [23] J. P. Perdew, A. Ruzsinszky, G. I. Csonka, O. A. Vydrov, G. E. Scuseria, L. A. Constantin, X. L. Zhou, and K. Burke, *Phys. Rev. Lett.* **100**, 136406 (2008).
- [24] G. Henkelman, B. P. Uberuaga, and H. Jonsson, *J. Chem. Phys.* **113**, 9901 (2000).
- [25] H. X. Xu, Y. N. Osetsky, and R. E. Stoller, *Phys. Rev. B* **84**, 132103 (2011).
- [26] H. X. Xu, Y. N. Osetsky, and R. E. Stoller, *J. Phys: Condens. Matter* **24**, 375402 (2012).
- [27] H. X. Xu, R. E. Stoller, L. K. Beland, and Y. N. Osetsky, *Computat. Mater. Sci.* **100**, 135 (2015).
- [28] H. X. Xu, R. E. Stoller, Y. N. Osetsky, and D. Terentyev, *Phys. Rev. Lett.* **110**, 265503 (2013).